

# Supplementary material for “Trace elements in olivine fingerprint the source of 2018 magmas and shed light on explosive-effusive eruption cycles at Kīlauea Volcano”

Adrien J. Mourey<sup>1</sup>, Thomas Shea<sup>1</sup>, Kendra J. Lynn<sup>2</sup>, Allan H. Lerner<sup>3</sup>, Sarah Lambert<sup>4</sup>, Fidel Costa<sup>5</sup>, Jeffrey Oalman<sup>6</sup>, R. Lopaka Lee<sup>2</sup>, Cheryl Gansecki<sup>7</sup>

<sup>1</sup>Department of Earth Sciences, University of Hawai‘i at Mānoa, Honolulu, HI, United States

<sup>2</sup>U.S. Geological Survey Hawaiian Volcano Observatory, HI, United States

<sup>3</sup>Department of Earth Sciences, University of Oregon, OR, United States

<sup>4</sup>Department of Geology and Geophysics, University of Utah, Salt Lake City, UT, United States

<sup>5</sup>Institut de Physique du Globe de Paris, France

<sup>6</sup>Earth Observatory of Singapore, Nanyang Technological University

<sup>7</sup>Geology Department, University of Hawai‘i at Hilo

## 1 Extended methods

### 1.1 Sample preparation

Lava and tephra were gently crushed and sieved to 1 mm, 500  $\mu\text{m}$  and 250  $\mu\text{m}$ . Olivine phenocrysts were picked. Phenocryst grains were individually mounted in 1-inch epoxy molds and polished until reaching the core to avoid sectioning effects. Polished sample surfaces were cleaned with ethanol and carbon coated before the electron probe analyses. Phenocrysts showed a variety of textures (euhedral or round, skeletal; Fig.S-1).

### 1.2 Electron probe micro-analysis (EPMA)

Relative precision ( $2\sigma$ ) based on repeat analyses of olivine Spring Water standard is better than 1% for Si, Fe, Mg, 2% for Mn, 9% for Cr. Accuracy is better than 1% for Si, Fe, Mg, Ca, Ni, about 2% for Mn, P, 9% for Cr. Relative precision ( $2\sigma$ ) based on repeat analyses of VG-2 standard is better than 1% for Si, Al, Fe, Mg, Ca, about 2% for Na, 4% for Ti, 6% for K, 11% for Mn, 20% for P. Accuracy is 1% for Si, Al, Mg, Ca, Na, K, about 2% for Ti, Fe, P, and 5% for Mn.

---

Corresponding author: Adrien J. Mourey, [amourey@hawaii.edu](mailto:amourey@hawaii.edu); ORCID 0000-0003-3498-9307

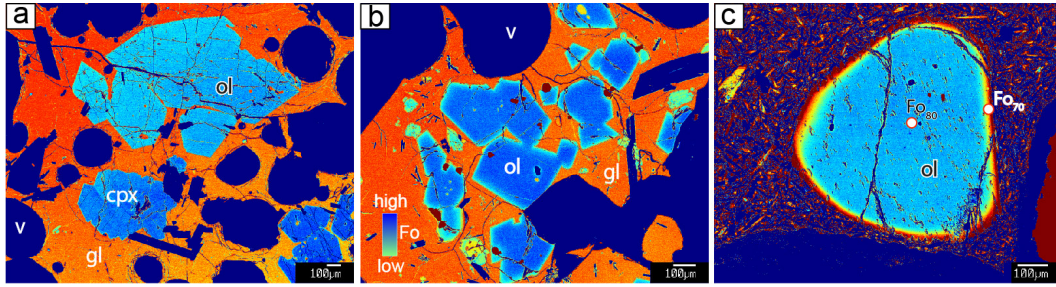


**Fig. S-1.** False colored backscattered electron image (BSE) image showing the olivine texture in 2018 at Pu‘u‘ō‘ō and LERZ. **(a)** Pu‘u‘ō‘ō sample collected 1 May, 2018 (KE61-3215S). Olivine is euhedral with slight no Fe-Mg zonation (forsterite  $Fo_{78-80}$ ); **(b)** Late fissure 8 sample collected 11 July, 2018 during the phase 3 (KE62-3311F). Olivine is euhedral with strong normal zonation (rims  $Fo_{77-84}$ , cores  $Fo_{77-90}$ ) **(c)** Early fissure 8 olivine collected 7 May, 2018. Olivine is round, normal zoned ( $Fo_{80}$  core and  $Fo_{70}$  rim). Not shown here: Halema‘uma‘u olivine collected in 2018 are euhedral with slight or no Fe-Mg zonation.

### 1.3 Laser ablation inductively coupled plasma mass spectrometry (LA-ICP MS)

For the olivine, the following isotopes were measured:  $^7\text{Li}$ ,  $^9\text{Be}$ ,  $^{23}\text{Na}$ ,  $^{27}\text{Al}$ ,  $^{31}\text{P}$ ,  $^{43}\text{Ca}$ ,  $^{45}\text{Sc}$ ,  $^{47}\text{Ti}$ ,  $^{51}\text{V}$ ,  $^{53}\text{Cr}$ ,  $^{55}\text{Mn}$ ,  $^{59}\text{Co}$ ,  $^{60}\text{Ni}$ ,  $^{63}\text{Cu}$ ,  $^{66}\text{Zn}$ ,  $^{69}\text{Ga}$ ,  $^{85}\text{Rb}$ ,  $^{88}\text{Sr}$ ,  $^{89}\text{Y}$ ,  $^{90}\text{Zr}$ ,  $^{93}\text{Nb}$ ,  $^{137}\text{Ba}$ ,  $^{140}\text{Ce}$ ,  $^{157}\text{Gd}$ ,  $^{172}\text{Yb}$ . For the matrix glass, the following isotopes were measured:  $^7\text{Li}$ ,  $^{31}\text{P}$ ,  $^{44}\text{Ca}$ ,  $^{45}\text{Sc}$ ,  $^{51}\text{V}$ ,  $^{53}\text{Cr}$ ,  $^{59}\text{Co}$ ,  $^{60}\text{Ni}$ ,  $^{85}\text{Rb}$ ,  $^{88}\text{Sr}$ ,  $^{89}\text{Y}$ ,  $^{90}\text{Zr}$ ,  $^{93}\text{Nb}$ ,  $^{137}\text{Ba}$ ,  $^{139}\text{La}$ ,  $^{140}\text{Ce}$ ,  $^{146}\text{Nd}$ ,  $^{147}\text{Sm}$ ,  $^{153}\text{Eu}$ ,  $^{157}\text{Gd}$ ,  $^{163}\text{Dy}$ ,  $^{166}\text{Er}$ ,  $^{172}\text{Yb}$ ,  $^{175}\text{Lu}$ ,  $^{178}\text{Hf}$ ,  $^{181}\text{Ta}$ ,  $^{208}\text{Pb}$ ,  $^{232}\text{Th}$ ,  $^{238}\text{U}$ . Total counting times were 5 ms for  $^{29}\text{Si}$  on olivine and  $^{44}\text{Ca}$  on matrix glass and 10 ms for all other isotopes. Data reduction was performed using the Trace Elements IS data reduction scheme of Iolite v. 3.6 (Paton et al., 2011). For all analyses, the synthetic basaltic glass GSD-1G was used as the primary calibration standard. For olivine and matrix glass, Si (based on stoichiometry) and Ca (determined by EPMA) were used as the internal standards, respectively. Reproducibility of the basaltic glass secondary reference materials BHVO-2G and BCR-2G are on the order of 1-3% relative standard deviation for most elements. The concentrations we obtained are within 10% of the GeoReM (Geological and Environmental Reference Materials) preferred values for all trace elements (except P and Al). We corrected for all trace elements the compositions of the unknown matrix glass and olivine phenocrysts using a correction factor based on the deviation of the measured secondary reference material concentrations from the GeoReM preferred concentrations. Because of the presence of microlites in some samples, we averaged the trace element compositions of  $\sim 10$  spots for each sample of matrix glass.

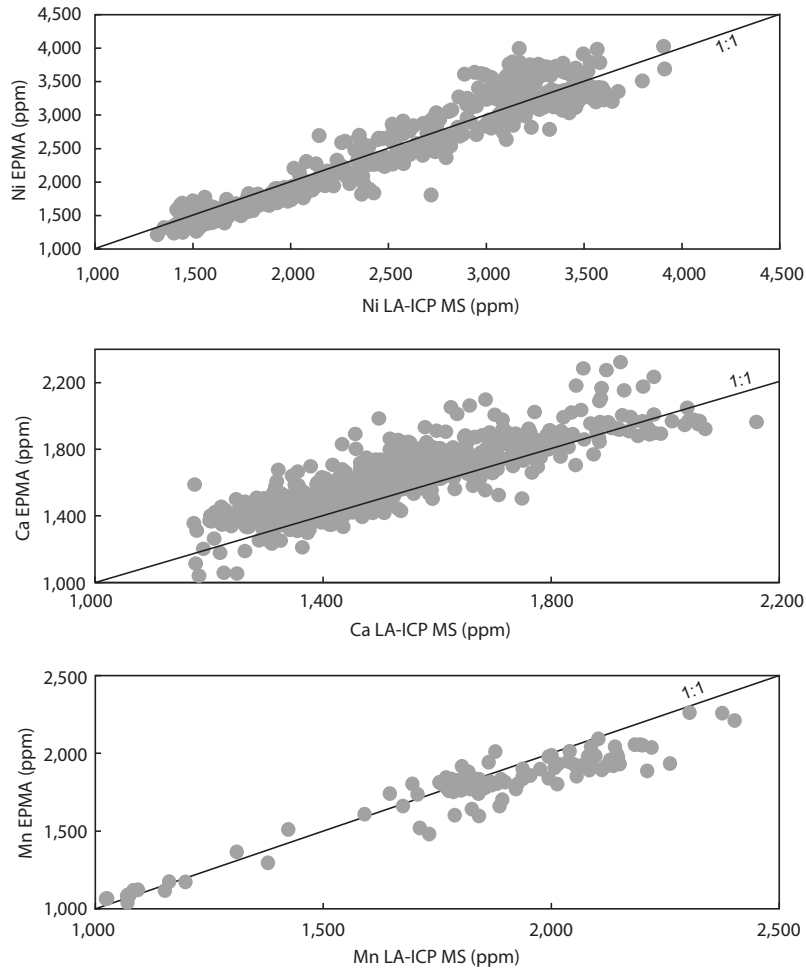


**Fig. S-2.** Measurements of Ni, Ca and Mn by Earth Observatory of Singapore (Nanyang Technological University) LA-ICP MS equipment compared to University of Hawai'i EPMA analyses conducted with high-probe current analysis procedure: 20 keV accelerating voltage and a 200 nA beam current with a diameter of 10  $\mu\text{m}$ .

## 2 Description of the Keanakāko'i Tephra units

Eruption style and intensity of the different eruptions producing the Keanakāko'i are diverse. The unit names and descriptions are from Swanson & Houghton, 2018.

### 2.1 Basal Reticulite

The basal reticulite of the Keanakāko'i tephra erupted in 1500 C.E. from different vents around the rim of the Kīlauea summit caldera (Swanson et al., 2012). The Keanakāko'i basal reticulite form a layer up to 65 cm along the caldera rim. The basal reticulite eruption style

consisted of a high fire fountain (>600 m) from a 200- to 300-m-deep caldera, allowing the preservation of golden-brown reticulites on the caldera rim (Swanson et al., 2012).

## **2.2 Unit D (units 7 and 11, ~1500-1650 C.E., section S07-39)**

Unit D is composed of phreatomagmatic vitric ash with also accretionary lapilli and Pele's hairs. This deposit is only found in the southern part of the caldera. There is no through-going marker bed, suggesting small eruption(s) and changing wind directions.

## **2.3 Unit E (Layer 6, ~1650 C.E.)**

The Unit E (layer 6) deposits of the Keanakākoī tephra consist of widely dispersed and coarse layer of fall scoria (McPhie et al., 1990). The deposit is spread ~20km from the vent to the southeast, suggesting plume heights of ~10-20 km (Swanson et al. 2012). This eruption is thought to be produced by a small-volume, explosive eruption (McPhie et al. 1990).

## **2.4 Unit G (unit 20, ~1650-1670 C.E.)**

This unit is a thinly bedded tephra layer composed of lithic-bearing vitric ash. This layer is below the circumferential lava flow (1-2m thick).

## **2.5 Unit K1 (Golden Pumice, early 1820's)**

The golden pumice eruption is thought to occurred early 1820's (Swanson & Houghton, 2018). It is composed of pumice with sparse lithic material produced by high lava fountains.

## **2.6 Unit K2 (Eastern Pumice, early 1820's)**

The eastern pumice is found on the southern side of Kīlauea's caldera. It is a mixture of Pele's hair, Pele's tears, basaltic pumice. Fieldwork and glass chemistry (Garcia et al., 2018) suggest that the eastern pumice overlies the golden pumice deposits.

## **3 Summary of the eruptive sequence during the 2018 Kīlauea eruption**

In early 2018, Pu'u'ō'ō and Halema'uma'u started to pressurize, and on April 30 a dike propagated beneath Pu'u'ō'ō towards the lower East Rift Zone (LERZ; Neal et al., 2019). On May 3, 24 fissures opened in the LERZ (Fig. S-3). Magma that erupted in the LERZ was

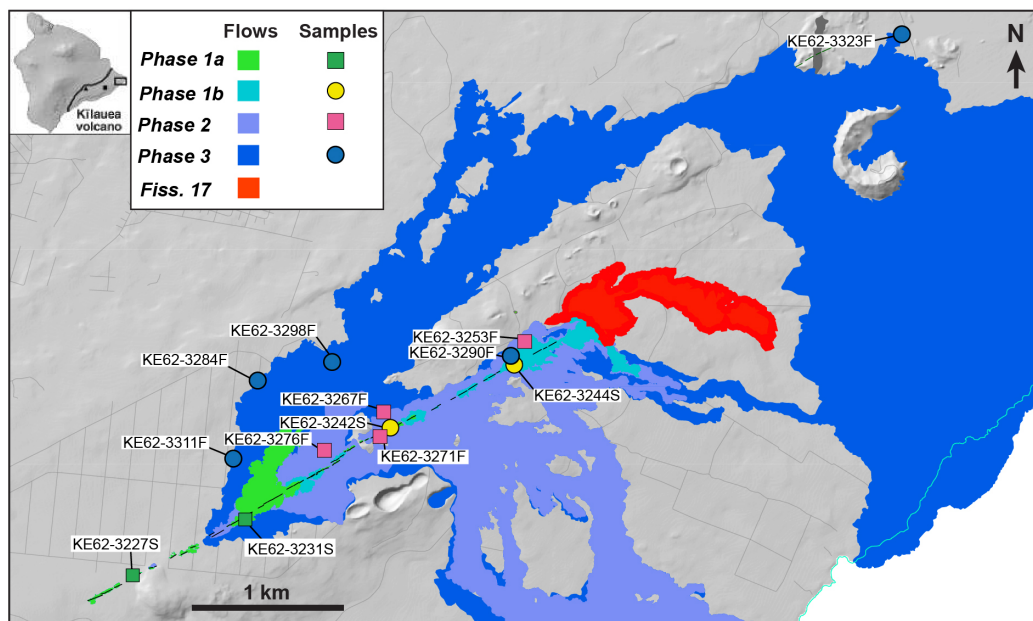


**Fig. S-3.** Map of lava flows and sample location for the 2018 Kilauea eruption. Flows are color-coded by eruptive sequence as in Gansecki et al., 2019. The pre-eruption coastline is shown in light blue. Map data: Esri, County of Hawai'i, Hawai'i Statewide GIS Program and USGS. No olivine was found in the fissure 17 lava flow. Any use of trade, firm, or product names is for descriptive purposes only and does not imply endorsement by the U.S. Government.

a mixture of (1) older and colder stored magma (high-Ti basalt erupted during 'phase 1' with 3.6-4.6 wt.% MgO in the matrix glass), (2) a basaltic-andesite to andesite magma erupted at fissure 17 (0.8-2.8 wt.% MgO) from 13 to 25 May 2018, and (3) hotter mafic magma (4.9-7.2 wt.% MgO in the matrix glass; 'phase 2 and 3'; Fig. S-3). In early 2018, Pu'u'ō'ō and Halema'uma'u started to pressurize, and on April 30 a dike propagated beneath Puuōō towards the lower East Rift Zone (LERZ; Neal et al., 2019). On May 3, 24 fissures opened in the LERZ (Fig. S-3). Magma that erupted in the LERZ was a mixture of (1) older and colder stored magma (high-Ti basalt erupted during 'phase 1' with 3.6-4.6 wt.% MgO in the matrix glass), (2) a basaltic-andesite to andesite magma erupted at fissure 17 (0.8-2.8 wt.% MgO) from 13 to 25 May 2018, and (3) hotter mafic magma (4.9-7.2 wt.% MgO in the matrix glass; 'phase 2 and 3'). On May 28, activity focused at fissure 8, which became the dominant vent until the eruption stopped (Neal et al., 2019). Fissure 8 produced 50-80 m lava fountains in late May and early June and fed a lava channel that traveled >10km to the ocean (Neal et al., 2019). Over 1.5 km<sup>3</sup> DRE (Dense Rock Equivalent) magma erupted from LERZ fissures during the 2018 crisis (Lerner et al., 2021).

## 4 Temporal evolution of olivine composition

### 4.1 2018 LERZ eruption

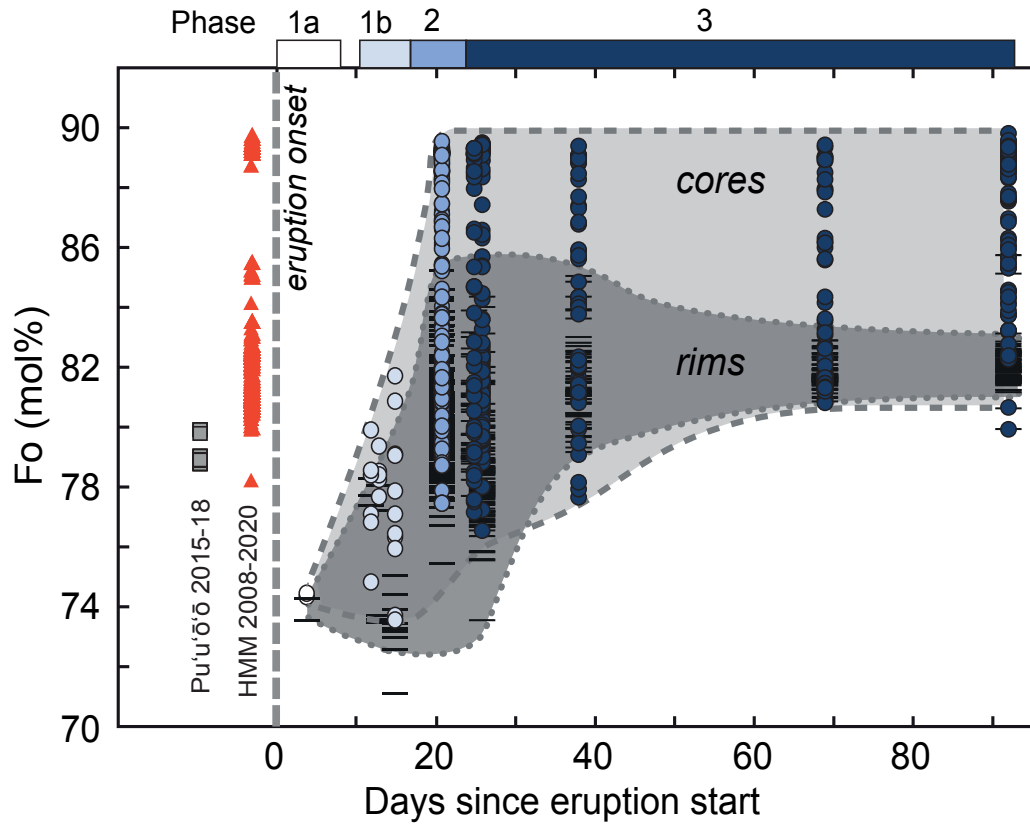


**Fig. S-4.** Fo content of olivine cores (filled symbols) and rims (lines) from the 2018 LERZ eruption and recent Pu'u'ō'ō and Halema'uma'u. High forsterite ( $Fo > 87$ ) olivine are observed in the LERZ 21 days after eruption onset and persists until the end of the eruption. Rims show a wide range in Fo the first month of the 2018 eruption and then converge towards  $Fo_{81-82}$ . Note the overlap in Fo content between the 2018 LERZ and recent Pu'u'ō'ō/Halema'uma'u olivine.

#### 4.2 Pu'u'ō'ō and Halema'uma'u olivine

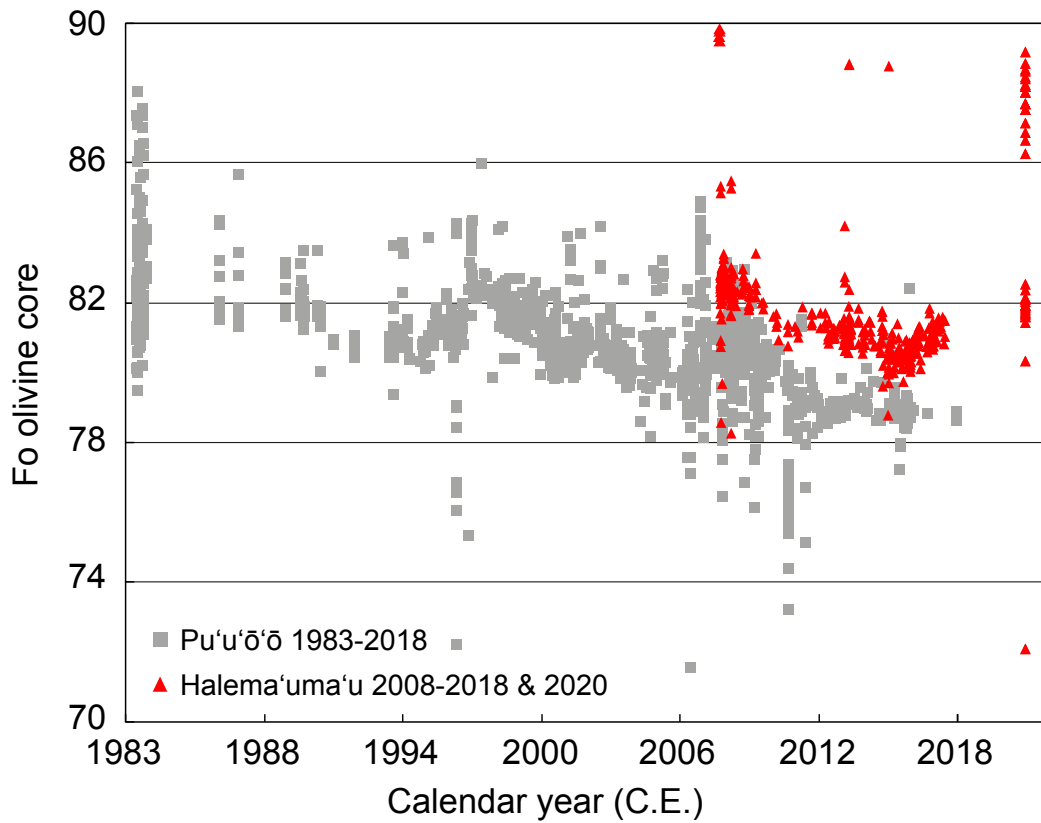


**Fig. S-5.** Pu'u'ō'ō and Halema'uma'u olivine core composition over time. Halema'uma'u olivine from the summit lava lake are on average 2 mol.% more forsteritic than the Pu'u'ō'ō olivine. The variation in olivine composition over time follows the same trend. The magma that crystallized at the Kīlauea summit lava lake (with ~ 7-7.5 wt.% MgO) was transported towards the East Rift Zone (Patrick et al., 2015) and progressively evolved to reach ~ 6.5 wt.% MgO in the Pu'u'ō'ō dike conduit. Note that most of the high Fo olivine (Fo>87) at Halema'uma'u were collected in 2008.

5 Comparison between Pu'u'ō'ō and LERZ 2018 olivine trace element compositions

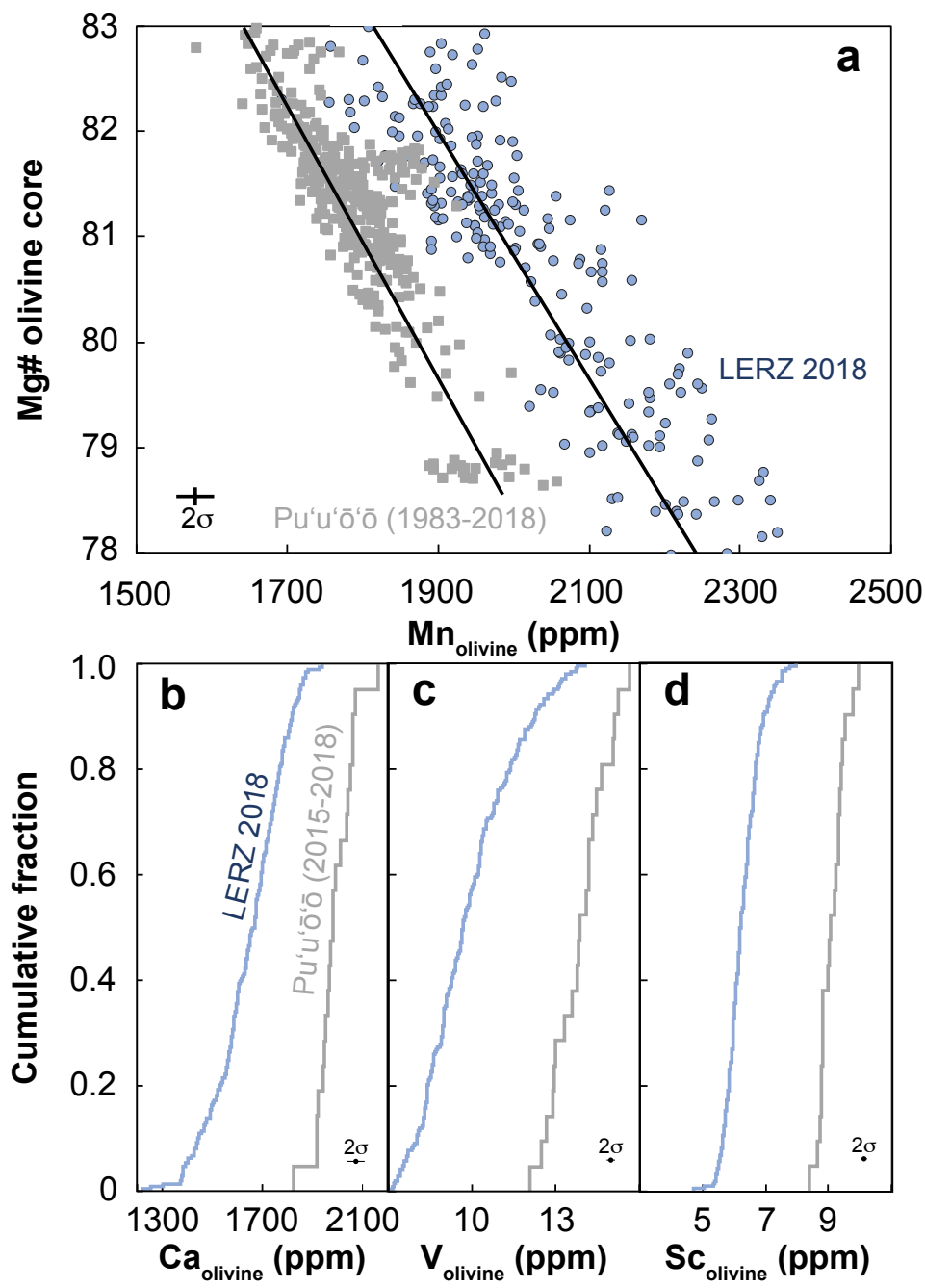


**Fig. S-6.** Selected trace elements (Mn, Ca, V, and Sc) that help distinguishing LERZ 2018 and Pu'u'ō'ō olivine. Note that Mn contents showed in (a) only represent Fo<sub>78-83</sub> olivine. Cumulative frequency plots in (b), (c) and (d) are all Fo contents measured in LERZ 2018 and Pu'u'ō'ō olivine.

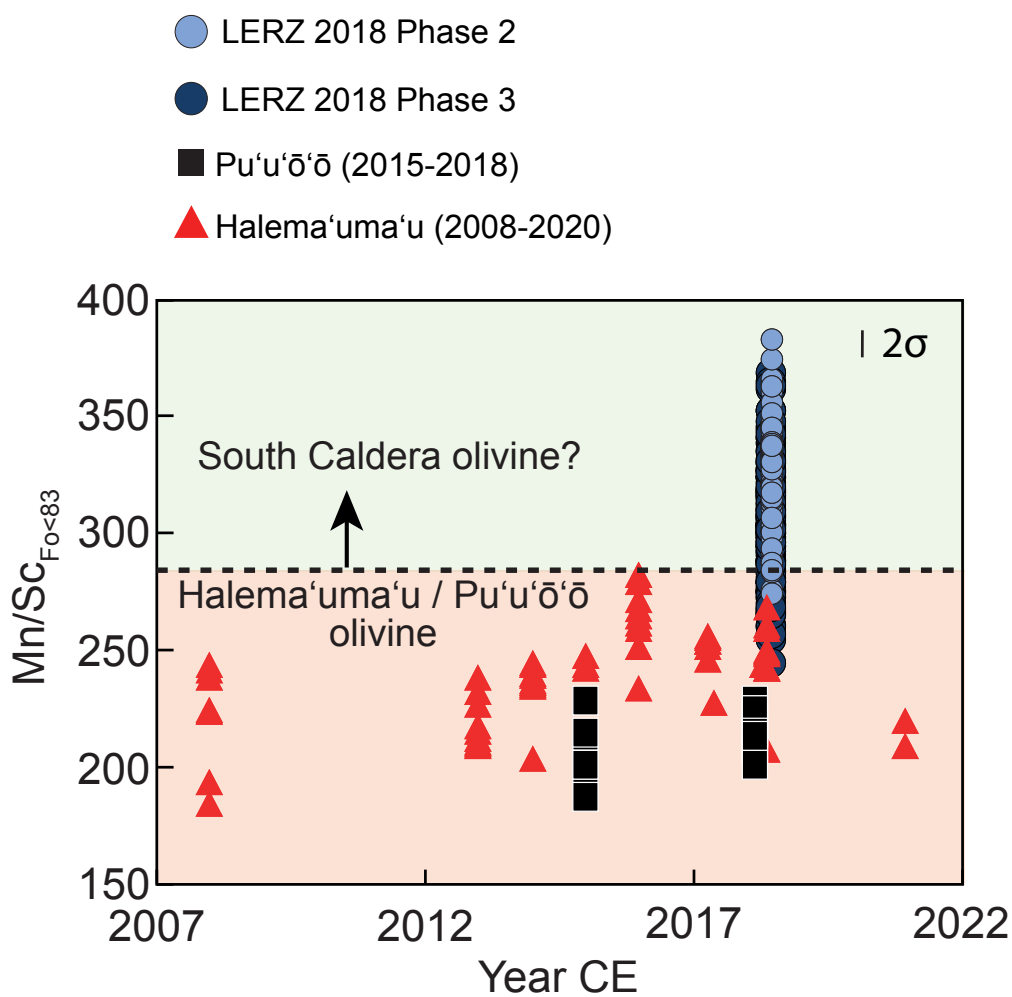


**Fig. S-7.** Mn/Sc values in Fo<83 olivine to discriminate olivine from the recent Pu'u'ō'ō (2015-2018) or Halema'uma'u (2008-2020) from the LERZ 2018 olivine.

6 Major and trace element ratios (FeO/V vs. Mn/Sc) useful to discriminate 2008-2020 Halema'uma'u, 2015-2018 Pu'u'ō'ō and LERZ 2018 olivine

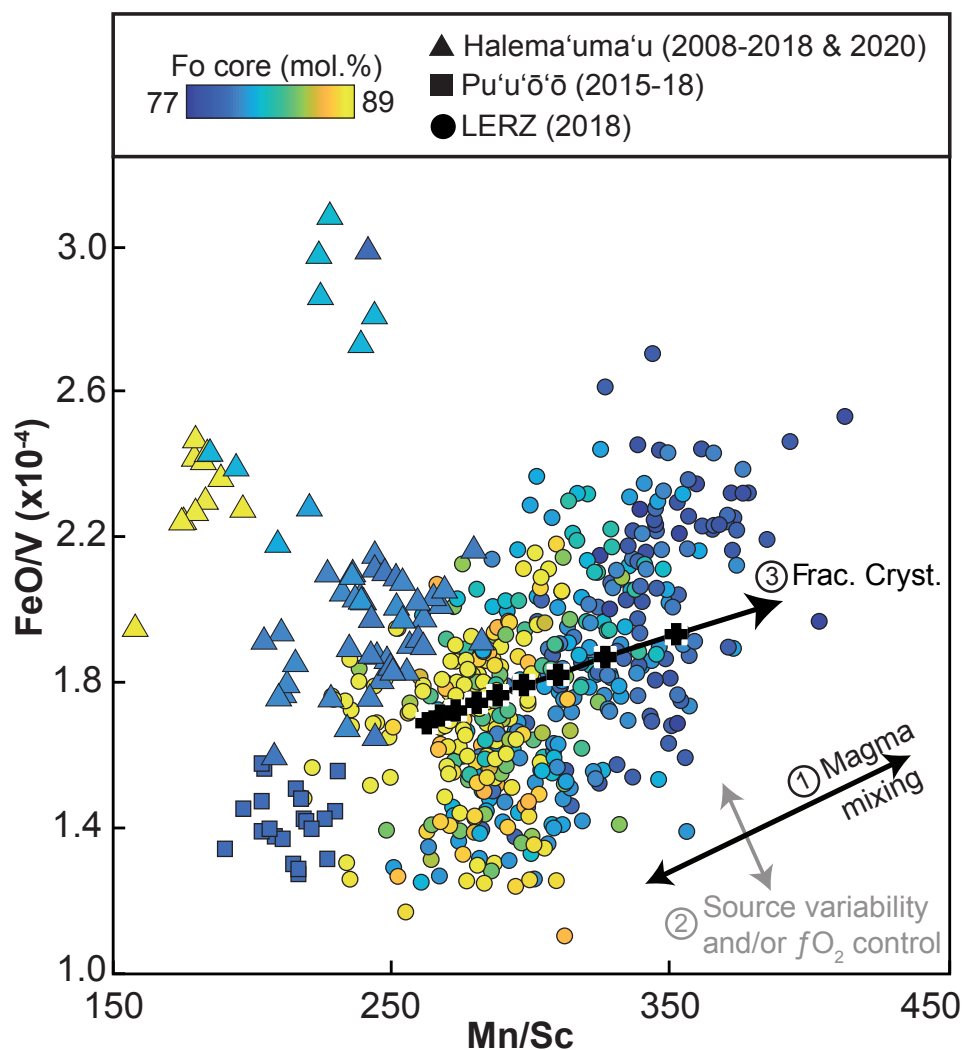


**Fig. S-8.** Pu'u'ō'ō olivine with Fo<sub>78-80</sub> is different from the Fo<sub>78-80</sub> of the Kīlauea 2018 LERZ eruption, and fractional crystallization cannot produce Pu'u'ō'ō olivine. The large variability in these ratios within 2018 LERZ olivine could result from (1) magma mixing and partial diffusive re-equilibration, (2) changes in the mantle source composition or in oxygen fugacity (fO<sub>2</sub>), and/or (3) fractional crystallization of olivine, orthopyroxene, clinopyroxene and plagioclase (crosses on the black line represent 10% increments).

## 7 Trace element concentrations in the 2018 LERZ olivine

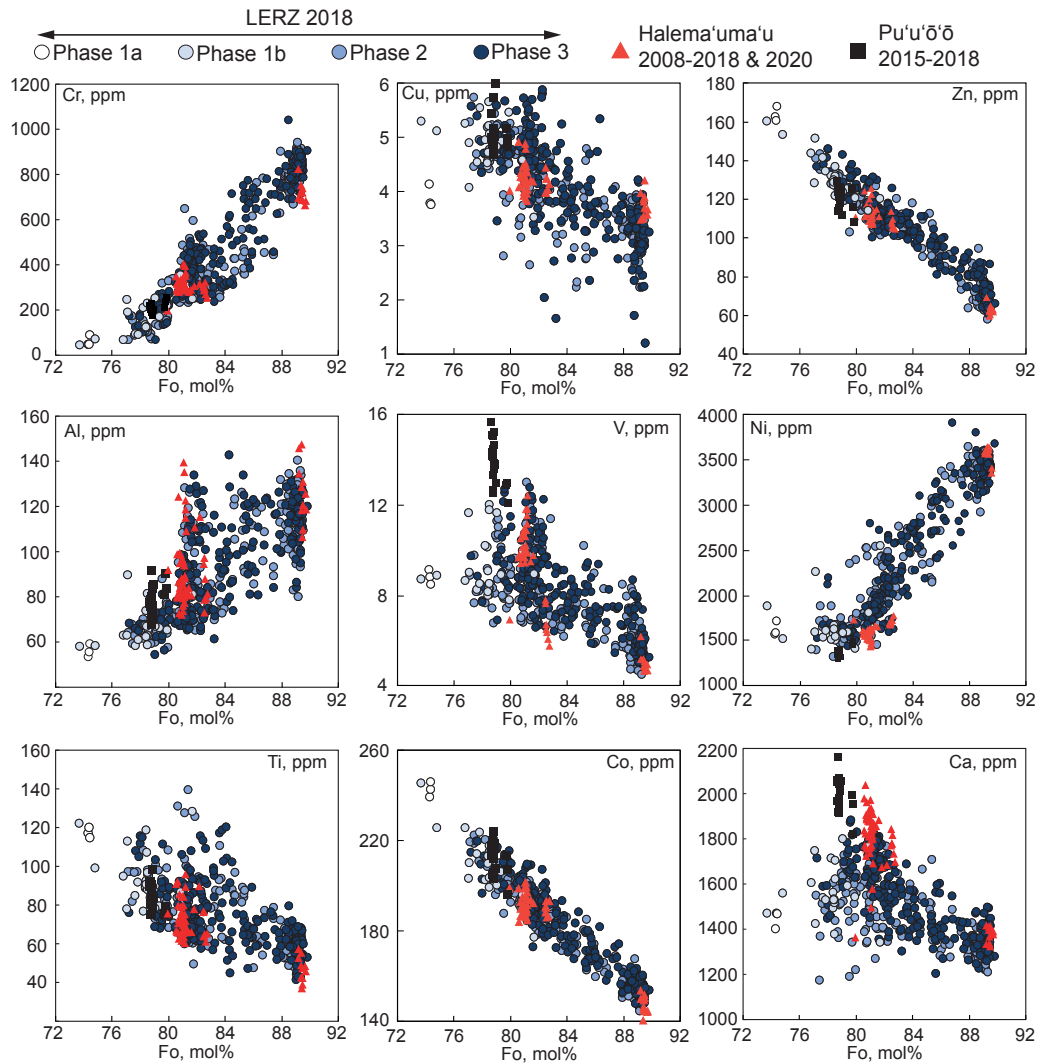


**Fig. S-9.** Trace element concentration in LERZ 2018, Pu'u'ō'ō and Halema'uma'u olivine. Note that olivine from these eruptions cannot be distinguished using these elements. Low-Fo olivine from the 2008-2018 Halema'uma'u eruption and 2020 Halema'uma'u eruption overlap in all these trace elements (also Sc, see Fig. 4).

## 8 Trace element concentrations in the 1500-early 1820's Keanakāko'i olivine

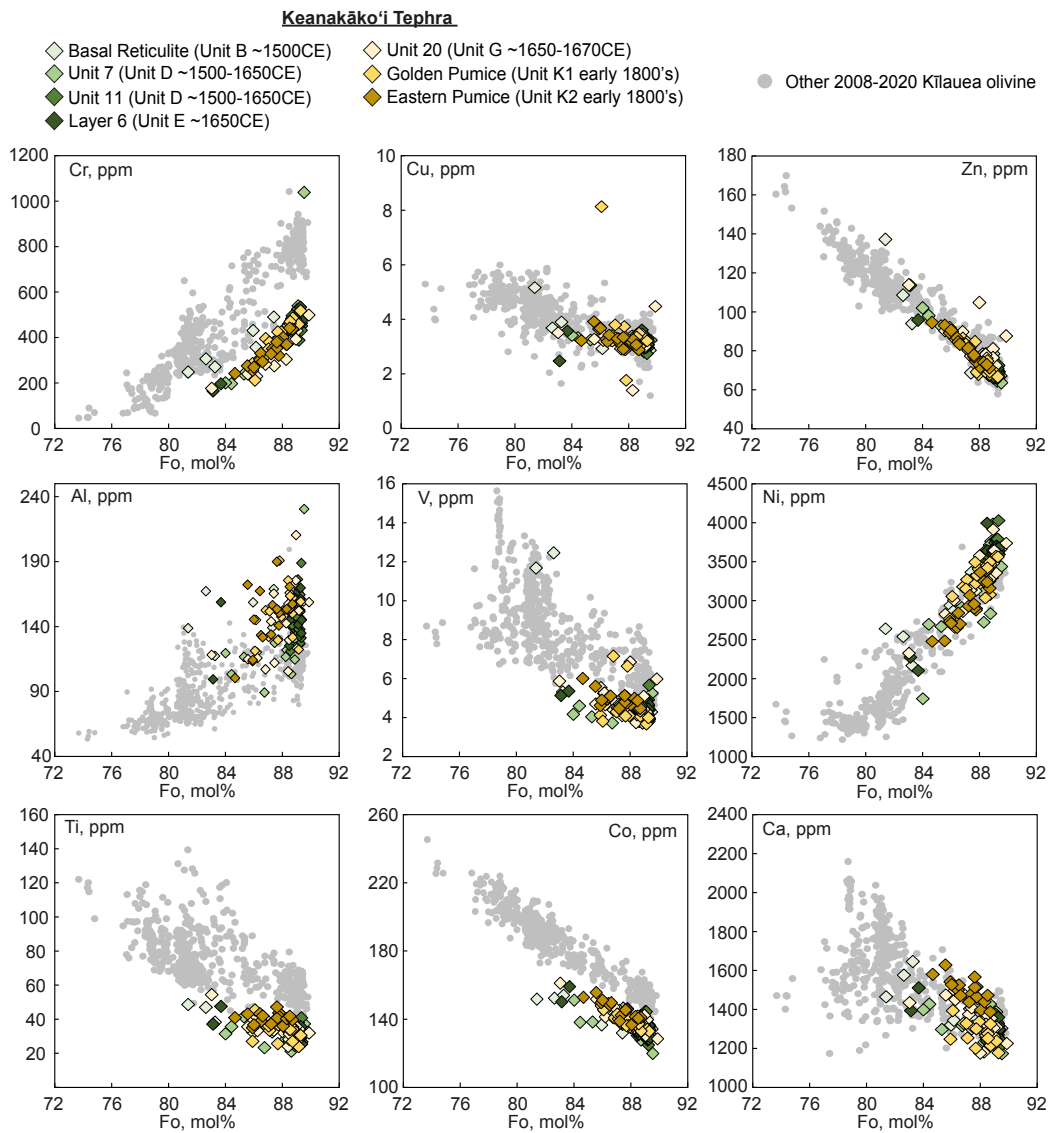


**Fig. S-10.** Trace element concentration in Keanakāko'i Tephra olivine, in comparison with LERZ 2018, Pu'ū'ō'ō and Halema'uma'u olivine (grey circles).

## 9 Vanadium in olivine oxybarometer

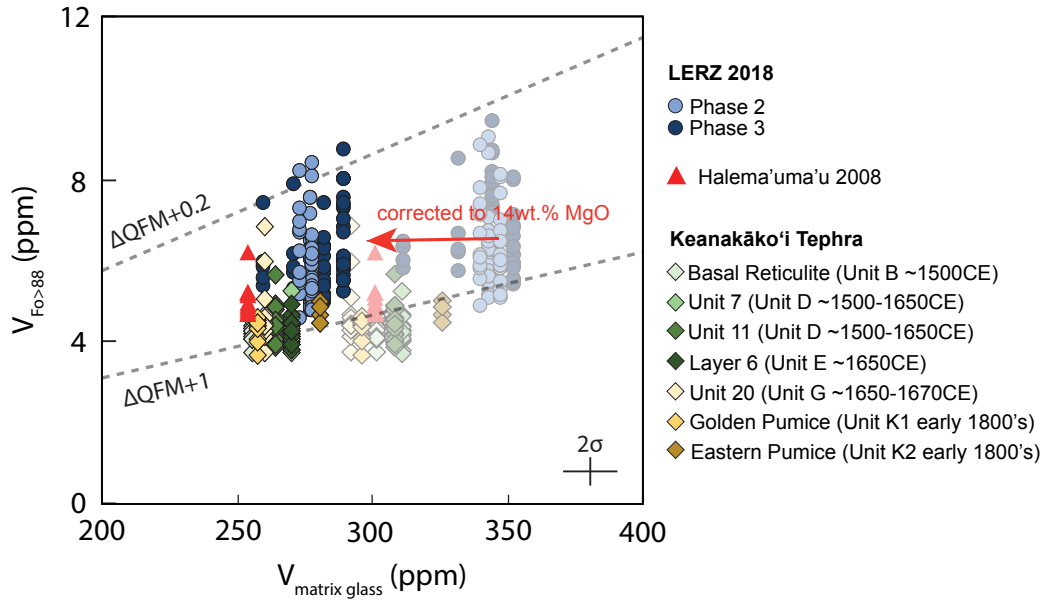


**Fig. S-11.** Vanadium (V) in olivine oxybarometer. Plot of V in high-Mg ( $Fo > 88$ ) olivine and V in matrix glasses. Oxygen fugacity contours are based on the model of Canil (2002). To convert from the NNO buffer to the FMQ buffer, we fixed  $T=1350^{\circ}\text{C}$  and  $P=800$  bars (3-5 km corresponding to the South Caldera depth at the Kīlauea summit, where most of the high-Mg olivine crystallize; Lerner et al., 2021). V in matrix glasses is an average of  $\sim 10$  spots for each sample. V in matrix glasses is then corrected for crystallization with Petrolog3 (Danyushevsky and Plechov, 2011) to primitive Kīlauea melts with  $\text{MgO}=14\text{wt.}\%$  (Lerner et al. 2021) and  $K_{Fe-Mg}^{ol/melt}=0.33$  and  $K_V^{ol/melt}=0.1$ . Corrected partition coefficients  $D_V = \left( \frac{\text{measured V in olivine}}{\text{corrected V in matrix glass}} \right)$  is used to calculate FMQ values (using the Canil, 2002 calibration).

## 10 Data references for olivine compositional histograms in Figure 2

### 10.1 Halema'uma'u

- USGS database
- This study

### 10.2 Pu'u'ō'ō

- Lynn, K.J., Shea, T., Garcia, M.O., 2017. Nickel variability in Hawaiian olivine: evaluating the relative contributions from mantle. *Am. Mineral.*102, 507–518.
- USGS database
- This study

### 10.3 Keanakāko'i Tephra

- Lynn, K.J., Garcia, M.O., Shea, T., Costa, F., Swanson, D.A., 2017. Timescales of mixing and storage for Keanakāko'i Tephra magmas (1500–1820 C.E.), Kīlauea Volcano, Hawai'i. *Contrib. Mineral. Petrol.* 172(9). doi:10.1007/s00410-017-1395-4

### 10.4 LERZ 2018

- Gansecki, C., Lopaka Lee, R., Shea, T., Lundblad, S.P., Hon, K., Parcheta, C., 2019. The tangled tale of Kīlauea's 2018 eruption as told by geochemical monitoring: *Science* 366, eaaz0147. <https://doi.org/10.1126/science.aaz0147>.
- Lerner, A.H., Wallace, P.J., Shea, T., Mourey, A.J. et al., 2021 The petrologic and degassing behavior of sulfur and other magmatic volatiles from the 2018 eruption of Kīlauea, Hawaii: melt concentrations, magma storage depths, and magma recycling. *Bull. Volc.* 83, 43. <https://doi.org/10.1007/s00445-021-01459-y>
- Wieser PE, Lamadrid H, MacLennan J, Edmonds M, Matthews S, Iacovino K, Jenner FE, Gansecki C, Trusdell F, Lee RL, Ilyinskaya E (2021) Reconstructing magma storage depths for the 2018 Kīlauean eruption from melt inclusion CO<sub>2</sub> contents: the importance of vapor bubbles. *Geochem Geophys Geosystems* 22:e2020GC009364. <https://doi.org/10.1029/2020GC009364>
- This study

## 10.5 Halema'uma'u 2020 lava lake eruption

- Lynn, K. J., Swanson, D. A., 2022. Olivine and glass chemistry record cycles of plumbing system recovery after summit collapse events at Kilauea Volcano, Hawai 'i. *J. Volc. Geo. Res.* 426, 107540.

**11 Starting composition and trace element mineral/melt partitioning coefficients used for the batch melting model (Fig. 8 in the main text)**

Table 1: Starting composition used for the batch melting model

Element	Starting composition (ppm)
Ni	1960
Co	106
Zn	56
Mn	1350
Sc	60

Table 2: Trace element mineral/melt partitioning coefficients used for the batch melting model

$K_d^{mineral/melt}$	Olivine	Orthopyroxene	Clinopyroxene	Garnet	Spinel
Ni	6 <sup>(1)</sup>	3.5 <sup>(2)</sup>	3.5 <sup>(3)</sup>	1 <sup>(4)</sup>	8 <sup>(5)</sup>
Co	1.5 <sup>(1)</sup>	1.3 <sup>(2)</sup>	1.06 <sup>(6)</sup>	0.9 <sup>(3)</sup>	2 <sup>(5)</sup>
Zn	1 <sup>(6)</sup>	0.68 <sup>(6)</sup>	0.5 <sup>(6)</sup>	0.9 <sup>(7)</sup>	5.2 <sup>(7)</sup>
Mn	1 <sup>(8)</sup>	1.4 <sup>(9)</sup>	0.7 <sup>(10)</sup>	3 <sup>(11)</sup>	2 <sup>(12)</sup>
Sc	0.25 <sup>(9,13)</sup>	1.29 <sup>(1)</sup>	3.1 <sup>(14)</sup>	6 <sup>(15)</sup>	0.5 <sup>(16)</sup>

References in parentheses: (1) Tuff and O'Neill, 2010; (2) Yao et al., 2012; (3) Girnis et al., 2013; (4) Suzuki et al., 2012; (5) Righter et al., 2006; (6) Le Roux et al., 2011; (7) Beunon et al., 2020; (8) Mallmann and O'Neill, 2013; (9) Laubier et al., 2014; (10) Dasgupta et al., 2009; (11) Dwarzski et al., 2006; (12) Toplis et al., 2002; (13) Davis et al., 2013; (14) Mollo et al., 2013; (15) Pertermann et al., 2004; (16) Wijbrans et al., 2015

## References

- Beunon, H.**, Mattielli, N., Doucet, L. S., Moine, B., and Debret, B., 2020. Mantle heterogeneity through Zn systematics in oceanic basalts: Evidence for a deep carbon cycling. *Earth-Science Reviews*, 103174. doi:10.1016/j.earscirev.2020.1031
- Dasgupta, R.**, Hirschmann, M.M., McDonough, W.F., Spiegelman, M., and Withers, A.C., 2009. Trace element partitioning between garnet lherzolite and carbonatite at 6.6 and 8.6 GPa with applications to the geochemistry of the mantle and of mantle-derived melts. *Chem. Geol.* 262(1-2), 57–77. doi:10.1016/j.chemgeo.2009.02.004
- Davis, F.A.**, Humayun, M., Hirschmann, M.M., and Cooper, R.S., 2013. Experimentally determined mineral/melt partitioning of first-row transition elements (FRTE) during partial melting of peridotite at 3GPa. *Geochim. Cosmochim. Acta* 104, 232–260. doi:10.1016/j.gca.2012.11.009
- Dwarzski, R.E.**, Draper, D.S., Shearer, C.K., and Agee, C.B., 2006. Experimental insights on crystal chemistry of high-Ti garnets from garnet-melt partitioning of rare-earth and high-field-strength elements. *Am. Mineral.* 91(10), 1536–1546. doi:10.2138/am.2006.2100
- Gansecki, C.**, Lopaka Lee, R., Shea, T., Lundblad, S.P., Hon, K., and Parcheta, C., 2019. The tangled tale of Kilauea’s 2018 eruption as told by geochemical monitoring: *Science* 366, eaaz0147. <https://doi.org/10.1126/science.aaz0147>.
- Garcia, M.O.**, Mucek, A.E., Lynn, K.J., Swanson, D.A., and Norman, M.D., 2018. Geochemical evolution of Keanakako’i Tephra, Kilauea Volcano, Hawai’i. *Field Volcanol.* 538:203
- Girnis, A.V.**, Bulatov, V.K., Brey, G.P., Gerdes, A., and Höfer, H.E., 2013. Trace element partitioning between mantle minerals and silico-carbonate melts at 6–12GPa and applications to mantle metasomatism and kimberlite genesis. *Lithos* 160-161, 183–200. doi:10.1016/j.lithos.2012.11.027
- Laubier, M.**, Grove, T.L., and Langmuir, C.H., 2014. Trace element mineral/melt partitioning for basaltic and basaltic andesitic melts: An experimental and laser ICP-MS study with application to the oxidation state of mantle source regions. *Earth Planet. Sci. Lett.* 392, 265–278. doi:10.1016/j.epsl.2014.01.053
- Le Roux, V.**, Dasgupta, R., and Lee, C.-T.A., 2011. Mineralogical heterogeneities in the Earth’s mantle: Constraints from Mn, Co, Ni and Zn partitioning during partial melting. *Earth Planet. Sci. Lett.* 307(3-4), 395–408. doi:10.1016/j.epsl.2011.05.014
- Lerner, A.H.**, Wallace, P.J., Shea, T., Mourey, A.J. et al., 2021 The petrologic and degassing behavior of sulfur and other magmatic volatiles from the 2018 eruption of Kilauea, Hawaii: melt concentrations, magma storage depths, and magma recycling. *Bull. Volc.* 83, 43. <https://doi.org/10.1007/s00445-021-01459-y>
- Mallmann, G.**, and O’Neill, H.S.C., 2013. Calibration of an Empirical Thermometer and Oxybarometer based on the Partitioning of Sc, Y and V between Olivine and Silicate Melt. *J. Petrol.* 54(5), 933–949. doi:10.1093/petrology/egt001
- McPhie, J.**, Walker J.P., and Christiansen, R.L., 1990. Phreatomagmatic and phreatic fall and surge deposits from explosions at Kilauea volcano, Hawaii, 1790 A.D.: Keanakakoi Ash Member. *Bull. Volc.* 52, 334–354. <https://doi.org/10.1007/BF00302047>

- Mollo, S.**, Blundy, J. D., Iezzi, G., Scarlato, P., and Langone, A., 2013. The partitioning of trace elements between clinopyroxene and trachybasaltic melt during rapid cooling and crystal growth. *Contrib. Mineral. Petrol.* 166(6), 1633–1654. doi:10.1007/s00410-013-0946-6
- Neal, C.A.**, et al., 2019, The 2018 rift eruption and summit collapse of Kilauea volcano: *Science* 363, 367-374. <https://doi.org/10.1126/science.aav7046>.
- Paton, C.**, Hellstrom, J., Paul, B., Woodhead, J., and Hergt, J., 2011. Iolite: Freeware for the visualisation and processing of mass spectrometric data. *J. Anal. Atomic Spec.* 26, 2508. <https://doi.org/10.1039/c1ja10172b>
- Patrick, M. R.**, Anderson, K. R., Poland, M. P., Orr, T. R., and Swanson, D. A., 2015. Lava lake level as a gauge of magma reservoir pressure and eruptive hazard. *Geology*, 43(9), 831–834. <https://doi.org/10.1130/g36896.1>
- Pertermann, M.**, Hirschmann, M.M., Hametner, K., Günther, D., and Schmidt, M.W., 2004. Experimental determination of trace element partitioning between garnet and silica-rich liquid during anhydrous partial melting of MORB-like eclogite. *Geochemistry, Geophysics, Geosystems* 5(5), n/a–n/a. doi:10.1029/2003gc000638
- Pertermann, M.**, Hirschmann, M.M., Hametner, K., Günther, D., and Schmidt, M.W., 2004. Experimental determination of trace element partitioning between garnet and silica-rich liquid during anhydrous partial melting of MORB-like eclogite. *Geochem. Geophys. Geosys.* 5(5), n/a–n/a. doi:10.1029/2003gc000638
- Righter, K.**, Leeman, W.P., and Hervig, R.L., 2006. Partitioning of Ni, Co and V between spinel-structured oxides and silicate melts: Importance of spinel composition. *Chem. Geol.* 227(1-2), 1–25. doi:10.1016/j.chemgeo.2005.05.011
- Suzuki, T.**, Hirata, T., Yokoyama, T.D., Imai, T., and Takahashi, E., 2012. Pressure effect on element partitioning between minerals and silicate melt: Melting experiments on basalt up to 20 GPa. *Physics of the Earth and Planet. Interiors* 208-209, 59–73. doi:10.1016/j.pepi.2012.07.008
- Swanson, D.A.**, Rose, T.R., Fiske, R.S., and McGeehin, J.P., 2012. Keanakāko‘i Tephra produced by 300 years of explosive eruptions following collapse of Kilauea’s caldera in about 1500 CE. *J. Volcanol. Geotherm. Res.* 215–216:8–25. <https://doi.org/10.1016/j.jvolgeorres.2011.11.009>
- Swanson, D.A.**, and Houghton, B.F., 2018. Products, processes, and implications of Keanakāko‘i volcanism, Kilauea Volcano, Hawai‘i. In: Poland MP, Garcia MO, Camp VE, Grunder A (eds) *Field volcanology: a tribute to disting career Don Swanson*, *Geol. Soc. Am. Spec. Pap.* 538, 159–190.
- Toplis, M.J.**, and Corgne, A., 2002. An experimental study of element partitioning between magnetite, clinopyroxene and iron-bearing silicate liquids with particular emphasis on vanadium. *Contrib. Mineral. Petrol.* 144(1), 22–37. doi:10.1007/s00410-002-0382-5
- Tuff, J.**, and O’Neill, H.S.C., 2010. The effect of sulfur on the partitioning of Ni and other first-row transition elements between olivine and silicate melt. *Geochim. Cosmochim. Acta* 74(21), 6180–6205. doi:10.1016/j.gca.2010.08.014
- Wijbrans, C.H.**, Klemme, S., Berndt, J., and Vollmer, C., 2015. Experimental determination of trace element partition coefficients between spinel and silicate melt: the influence

of chemical composition and oxygen fugacity. *Contrib. Mineral. Petrol.* 169(4). doi:10.1007/s00410-015-1128-5

**Yao, L.**, Sun, C., and Liang, Y., 2012. A parameterized model for REE distribution between low-Ca pyroxene and basaltic melts with applications to REE partitioning in low-Ca pyroxene along a mantle adiabat and during pyroxenite-derived melt and peridotite interaction. *Contrib. Mineral. Petrol.* 164(2), 261–280. doi:10.1007/s00410-012-0737-5